



# Angiographic and structural imaging using high axial resolution fiber-based visible-light OCT

SHAOHUA PI,<sup>1,3</sup> ACNER CAMINO,<sup>1,3</sup> MIAO ZHANG,<sup>2</sup> WILLIAM CEPURNA,<sup>1</sup>  
GANGJUN LIU,<sup>1</sup> DAVID HUANG,<sup>1</sup> JOHN MORRISON,<sup>1</sup> AND YALI JIA<sup>1,\*</sup>

<sup>1</sup>Casey Eye Institute, Oregon Health & Science University, Portland, OR, USA

<sup>2</sup>Optovue Inc. 2800 Bayview Dr., Fremont, CA 94538, USA

<sup>3</sup>These authors contributed equally to this work

\*jiaya@ohsu.edu

**Abstract:** Optical coherence tomography using visible-light sources can increase the axial resolution without the need for broader spectral bandwidth. Here, a high-resolution, fiber-based, visible-light optical coherence tomography system is built and used to image normal retina in rats and blood vessels in chicken embryo. In the rat retina, accurate segmentation of retinal layer boundaries and quantification of layer thicknesses are accomplished. Furthermore, three distinct capillary plexuses in the retina and the choriocapillaris are identified and the characteristic pattern of the nerve fiber layer thickness in rats is revealed. In the chicken embryo model, the microvascular network and a venous bifurcation are examined and the ability to identify and segment large vessel walls is demonstrated.

© 2017 Optical Society of America

**OCIS codes:** (110.4500) Optical coherence tomography; (170.2655) Functional monitoring and imaging; (170.4470) Ophthalmology; (100.2980) Image enhancement.

## References and links

1. J. M. Schmitt, "Optical coherence tomography (OCT): a review," *IEEE J. Sel. Top. Quantum Electron.* **5**(4), 1205–1215 (1999).
2. D. Huang, E. A. Swanson, C. P. Lin, J. S. Schuman, W. G. Stinson, W. Chang, M. R. Hee, T. Flotte, K. Gregory, C. A. Puliafito, and et, "Optical coherence tomography," *Science* **254**(5035), 1178–1181 (1991).
3. A. M. Zysk, F. T. Nguyen, A. L. Oldenburg, D. L. Marks, and S. A. Boppart, "Optical coherence tomography: a review of clinical development from bench to bedside," *J. Biomed. Opt.* **12**, 051403 (2007).
4. M. Wojtkowski, R. Leitgeb, A. Kowalczyk, T. Bajraszewski, and A. F. Fercher, "In vivo human retinal imaging by Fourier domain optical coherence tomography," *J. Biomed. Opt.* **7**(3), 457–463 (2002).
5. W. Drexler, U. Morgner, R. K. Ghanta, F. X. Kärtner, J. S. Schuman, and J. G. Fujimoto, "Ultrahigh-resolution ophthalmic optical coherence tomography," *Nat. Med.* **7**(4), 502–507 (2001).
6. V. J. Srinivasan, D. C. Adler, Y. Chen, I. Gorczynska, R. Huber, J. S. Duker, J. S. Schuman, and J. G. Fujimoto, "Ultrahigh-speed optical coherence tomography for three-dimensional and en face imaging of the retina and optic nerve head," *Invest. Ophthalmol. Vis. Sci.* **49**(11), 5103–5110 (2008).
7. S. S. Gao, Y. Jia, M. Zhang, J. P. Su, G. Liu, T. S. Hwang, S. T. Bailey, and D. Huang, "Optical Coherence Tomography Angiography," *Invest. Ophthalmol. Vis. Sci.* **57**(9), 27–36 (2016).
8. D. Huang, Y. Jia, and S. S. Gao, "Principles of optical coherence tomography angiography," *OCT Angiography Atlas*. New Delhi, India: Jaypee Brothers Medical Publishers, 3–7 (2015).
9. Y. Jia, O. Tan, J. Tokayer, B. Potsaid, Y. Wang, J. J. Liu, M. F. Kraus, H. Subhash, J. G. Fujimoto, J. Hornegger, and D. Huang, "Split-spectrum amplitude-decorrelation angiography with optical coherence tomography," *Opt. Express* **20**(4), 4710–4725 (2012).
10. G. Liu, Y. Jia, A. D. Pechauer, R. Chandwani, and D. Huang, "Split-spectrum phase-gradient optical coherence tomography angiography," *Biomed. Opt. Express* **7**(8), 2943–2954 (2016).
11. R. K. Wang, L. An, P. Francis, and D. J. Wilson, "Depth-resolved imaging of capillary networks in retina and choroid using ultrahigh sensitive optical microangiography," *Opt. Lett.* **35**(9), 1467–1469 (2010).
12. Y. Jia, S. T. Bailey, T. S. Hwang, S. M. McClintic, S. S. Gao, M. E. Pennesi, C. J. Flaxel, A. K. Lauer, D. J. Wilson, J. Hornegger, J. G. Fujimoto, and D. Huang, "Quantitative optical coherence tomography angiography of vascular abnormalities in the living human eye," *Proc. Natl. Acad. Sci. U.S.A.* **112**(18), E2395–E2402 (2015).
13. Y. Jia, J. C. Morrison, J. Tokayer, O. Tan, L. Lombardi, B. Baumann, C. D. Lu, W. Choi, J. G. Fujimoto, and D. Huang, "Quantitative OCT angiography of optic nerve head blood flow," *Biomed. Opt. Express* **3**(12), 3127–3137 (2012).

14. Y. Jia, E. Wei, X. Wang, X. Zhang, J. C. Morrison, M. Parikh, L. H. Lombardi, D. M. Gattey, R. L. Armour, B. Edmunds, M. F. Kraus, J. G. Fujimoto, and D. Huang, "Optical coherence tomography angiography of optic disc perfusion in glaucoma," *Ophthalmology* **121**(7), 1322–1332 (2014).
15. C.-L. Chen, A. Zhang, K. D. Bojikian, J. C. Wen, Q. Zhang, C. Xin, R. C. Mudumbai, M. A. Johnstone, P. P. Chen, and R. K. Wang, "Peripapillary Retinal Nerve Fiber Layer Vascular Microcirculation in Glaucoma Using Optical Coherence Tomography-Based," *Invest. Ophthalmol. Vis. Sci.* **57**(9), 475–485 (2016).
16. L. Liu, S. S. Gao, S. T. Bailey, D. Huang, D. Li, and Y. Jia, "Automated choroidal neovascularization detection algorithm for optical coherence tomography angiography," *Biomed. Opt. Express* **6**(9), 3564–3576 (2015).
17. Y. Jia, S. T. Bailey, D. J. Wilson, O. Tan, M. L. Klein, C. J. Flaxel, B. Potsaid, J. J. Liu, C. D. Lu, M. F. Kraus, J. G. Fujimoto, and D. Huang, "Quantitative optical coherence tomography angiography of choroidal neovascularization in age-related macular degeneration," *Ophthalmology* **121**(7), 1435–1444 (2014).
18. T. S. Hwang, S. S. Gao, L. Liu, A. K. Lauer, S. T. Bailey, C. J. Flaxel, D. J. Wilson, D. Huang, and Y. Jia, "Automated quantification of capillary nonperfusion using optical coherence tomography angiography in diabetic retinopathy," *JAMA Ophthalmol.* **134**(4), 367–373 (2016).
19. T. S. Hwang, M. Zhang, K. Bhavsar, X. Zhang, J. P. Campbell, P. Lin, S. T. Bailey, C. J. Flaxel, A. K. Lauer, D. J. Wilson, D. Huang, and Y. Jia, "Visualization of 3 distinct retinal plexuses by projection-resolved optical coherence tomography angiography in diabetic retinopathy," *JAMA Ophthalmol.* **134**(12), 1411–1419 (2016).
20. P. Li and R. K. Wang, "Optical coherence tomography provides an ability to assess mechanical property of cardiac wall of developing outflow tract in embryonic heart in vivo," *J. Biomed. Opt.* **17**(12), 120502 (2012).
21. J. G. Fujimoto, C. Pitris, S. A. Boppart, and M. E. Brezinski, "Optical coherence tomography: an emerging technology for biomedical imaging and optical biopsy," *Neoplasia* **2**(1-2), 9–25 (2000).
22. M. R. Hee, J. A. Izatt, E. A. Swanson, D. Huang, J. S. Schuman, C. P. Lin, C. A. Puliafito, and J. G. Fujimoto, "Optical coherence tomography of the human retina," *Arch. Ophthalmol.* **113**(3), 325–332 (1995).
23. J. Fujimoto and E. Swanson, "The Development, Commercialization, and Impact of Optical Coherence Tomography History of Optical Coherence Tomography," *Invest. Ophthalmol. Vis. Sci.* **57**(9), 1–13 (2016).
24. A. C. Sull, L. N. Vuong, L. L. Price, V. J. Srinivasan, I. Gorczynska, J. G. Fujimoto, J. S. Schuman, and J. S. Duker, "Comparison of Spectral/Fourier Domain Optical Coherence Tomography Instruments for Assessment of Normal Macular Thickness," *Retina* **30**(2), 235–245 (2010).
25. G. Bartsch, D.-U. Bartsch, F. Viola, F. Mojana, M. Pellegrini, K. I. Hartmann, E. Benatti, S. Leicht, R. Ratiglia, G. Staurengi, R. N. Weinreb, and W. R. Freeman, "Accuracy of the Heidelberg Spectralis in the alignment between near-infrared image and tomographic scan in a model eye: a multicenter study," *Am. J. Ophthalmol.* **156**(3), 588–592 (2013).
26. P. J. Rosenfeld, M. K. Durbin, L. Roisman, F. Zheng, A. Miller, G. Robbins, K. B. Schaal, and G. Gregori, "ZEISS Angioplex™ Spectral Domain Optical Coherence Tomography Angiography: Technical Aspects," *Dev. Ophthalmol.* **56**, 18–29 (2016).
27. M. Wojtkowski, V. Srinivasan, T. Ko, J. Fujimoto, A. Kowalczyk, and J. Duker, "Ultrahigh-resolution, high-speed, Fourier domain optical coherence tomography and methods for dispersion compensation," *Opt. Express* **12**(11), 2404–2422 (2004).
28. J. Barrick, A. Doblas, M. R. Gardner, P. R. Sears, L. E. Ostrowski, and A. L. Oldenburg, "High-speed and high-sensitivity parallel spectral-domain optical coherence tomography using a supercontinuum light source," *Opt. Lett.* **41**(24), 5620–5623 (2016).
29. J. Yi, S. Chen, V. Backman, and H. F. Zhang, "In vivo functional microangiography by visible-light optical coherence tomography," *Biomed. Opt. Express* **5**(10), 3603–3612 (2014).
30. J. Yi, W. Liu, S. Chen, V. Backman, N. Sheibani, C. M. Sorenson, A. A. Fawzi, R. A. Linsenmeier, and H. F. Zhang, "Visible light optical coherence tomography measures retinal oxygen metabolic response to systemic oxygenation," *Light Sci. Appl.* **4**(9), e334 (2015).
31. S. P. Chong, C. W. Merkle, C. Leahy, H. Radhakrishnan, and V. J. Srinivasan, "Quantitative microvascular hemoglobin mapping using visible light spectroscopic Optical Coherence Tomography," *Biomed. Opt. Express* **6**(4), 1429–1450 (2015).
32. S. Chen, J. Yi, W. Liu, V. Backman, and H. F. Zhang, "Monte Carlo investigation of optical coherence tomography retinal oximetry," *IEEE Trans. Biomed. Eng.* **62**(9), 2308–2315 (2015).
33. S. Chen, X. Shu, J. Yi, A. Fawzi, and H. F. Zhang, "Dual-band optical coherence tomography using a single supercontinuum laser source," *J. Biomed. Opt.* **21**(6), 066013 (2016).
34. W. Drexler and J. G. Fujimoto, *Optical Coherence Tomography: Technology and Applications* (Springer Science & Business Media, 2008).
35. S. L. Jacques, "Optical properties of biological tissues: a review," *Phys. Med. Biol.* **58**(11), R37–R61 (2013).
36. J. A. Izatt, M. A. Choma, and A.-H. Dhalla, "Theory of optical coherence tomography," *Optical Coherence Tomography: Technology and Applications* **2015**, 65–94 (2015).
37. W. Drexler, "Ultrahigh-resolution optical coherence tomography," *J. Biomed. Opt.* **9**(1), 47–74 (2004).
38. Y. Ding, B. Aredo, X. Zhong, C. X. Zhao, and R. L. Ufret-Vincenty, "Increased susceptibility to fundus camera-delivered light-induced retinal degeneration in mice deficient in oxidative stress response proteins," *Exp. Eye Res.* **159**, 58–68 (2017).
39. V. J. Srinivasan, T. H. Ko, M. Wojtkowski, M. Carvalho, A. Clermont, S.-E. Bursell, Q. H. Song, J. Lem, J. S. Duker, J. S. Schuman, and J. G. Fujimoto, "Noninvasive volumetric imaging and morphometry of the rodent

- retina with high-speed, ultrahigh-resolution optical coherence tomography,” *Invest. Ophthalmol. Vis. Sci.* **47**(12), 5522–5528 (2006).
40. J. Yi, S. Chen, X. Shu, A. A. Fawzi, and H. F. Zhang, “Human retinal imaging using visible-light optical coherence tomography guided by scanning laser ophthalmoscopy,” *Biomed. Opt. Express* **6**(10), 3701–3713 (2015).
  41. Y. Watanabe and T. Itagaki, “Real-time display on Fourier domain optical coherence tomography system using a graphics processing unit,” *J. Biomed. Opt.* **14**, 060506 (2009).
  42. M. Zhang, J. Wang, A. D. Pechauer, T. S. Hwang, S. S. Gao, L. Liu, L. Liu, S. T. Bailey, D. J. Wilson, D. Huang, and Y. Jia, “Advanced image processing for optical coherence tomographic angiography of macular diseases,” *Biomed. Opt. Express* **6**(12), 4661–4675 (2015).
  43. R. F. Spaide, J. G. Fujimoto, and N. K. Waheed, “Image Artifacts in Optical Coherence Tomography Angiography,” *Retina* **35**(11), 2163–2180 (2015).
  44. A. Camino, M. Zhang, S. S. Gao, T. S. Hwang, U. Sharma, D. J. Wilson, D. Huang, and Y. Jia, “Evaluation of artifact reduction in optical coherence tomography angiography with real-time tracking and motion correction technology,” *Biomed. Opt. Express* **7**(10), 3905–3915 (2016).
  45. K. Adachi, S. Takahashi, K. Yamauchi, N. Mounai, R. Tanabu, and M. Nakazawa, “Optical Coherence Tomography of Retinal Degeneration in Royal College of Surgeons Rats and Its Correlation with Morphology and Electroretinography,” *PLoS One* **11**(9), e0162835 (2016).
  46. R. C. Ryals, M. D. Andrews, S. Datta, A. S. Coyner, C. M. Fischer, Y. Wen, M. E. Pennesi, and T. J. McGill, “Long-term Characterization of Retinal Degeneration in Royal College of Surgeons Rats Using Spectral-Domain Optical Coherence Tomography,” *Invest. Ophthalmol. Vis. Sci.* **58**(3), 1378–1386 (2017).
  47. A. Berger, S. Cavallero, E. Dominguez, P. Barbe, M. Simonutti, J.-A. Sahel, F. Sennlaub, W. Raoul, M. Paques, and A.-P. Bemelmans, “Spectral-Domain Optical Coherence Tomography of the Rodent Eye: Highlighting Layers of the Outer Retina Using Signal Averaging and Comparison with Histology,” *PLoS One* **9**(5), e96494 (2014).
  48. F. A. Medeiros, L. M. Zangwill, C. Bowd, R. M. Vessani, R. Susanna, Jr., and R. N. Weinreb, “Evaluation of retinal nerve fiber layer, optic nerve head, and macular thickness measurements for glaucoma detection using optical coherence tomography,” *Am. J. Ophthalmol.* **139**(1), 44–55 (2005).
  49. S. Kirbas, K. Turkyilmaz, O. Anlar, A. Tufekci, and M. Durmus, “Retinal nerve fiber layer thickness in patients with Alzheimer disease,” *J. Neuroophthalmol.* **33**(1), 58–61 (2013).
  50. R. Inzelberg, J. A. Ramirez, P. Nisipeanu, and A. Ophir, “Retinal nerve fiber layer thinning in Parkinson disease,” *Vision Res.* **44**(24), 2793–2797 (2004).
  51. J. Wang, M. Zhang, T. S. Hwang, S. T. Bailey, D. Huang, D. J. Wilson, and Y. Jia, “Reflectance-based projection-resolved optical coherence tomography angiography,” *Biomed. Opt. Express* **8**(3), 1536–1548 (2017).
  52. J. P. Campbell, M. Zhang, T. S. Hwang, S. T. Bailey, D. J. Wilson, Y. Jia, and D. Huang, “Detailed vascular anatomy of the human retina by projection-resolved optical coherence tomography angiography,” *Sci. Rep.* **7**, 42201 (2017).
  53. M. Zhang, T. S. Hwang, J. P. Campbell, S. T. Bailey, D. J. Wilson, D. Huang, and Y. Jia, “Projection-resolved optical coherence tomographic angiography,” *Biomed. Opt. Express* **7**(3), 816–828 (2016).
  54. Z. Zhi, W. Cepurna, E. Johnson, H. Jayaram, J. Morrison, and R. K. Wang, “Evaluation of the effect of elevated intraocular pressure and reduced ocular perfusion pressure on retinal capillary bed filling and total retinal blood flow in rats by OMAG/OCT,” *Microvasc. Res.* **101**, 86–95 (2015).
  55. Z. Zhi, W. O. Cepurna, E. C. Johnson, J. C. Morrison, and R. K. Wang, “Impact of intraocular pressure on changes of blood flow in the retina, choroid, and optic nerve head in rats investigated by optical microangiography,” *Biomed. Opt. Express* **3**(9), 2220–2233 (2012).
  56. M. Paques, R. Tadayoni, R. Sercombe, P. Laurent, O. Genevois, A. Gaudric, and E. Vicaut, “Structural and hemodynamic analysis of the mouse retinal microcirculation,” *Invest. Ophthalmol. Vis. Sci.* **44**(11), 4960–4967 (2003).
  57. Z. Ma, A. Liu, X. Yin, A. Troyer, K. Thornburg, R. K. Wang, and S. Rugonyi, “Measurement of absolute blood flow velocity in outflow tract of HH18 chicken embryo based on 4D reconstruction using spectral domain optical coherence tomography,” *Biomed. Opt. Express* **1**(3), 798–811 (2010).
  58. T. F. Sherman, “On connecting large vessels to small. The meaning of Murray’s law,” *J. Gen. Physiol.* **78**(4), 431–453 (1981).
  59. Z. Chen, T. E. Milner, S. Srinivas, X. Wang, A. Malekafzali, M. J. van Gemert, and J. S. Nelson, “Noninvasive imaging of in vivo blood flow velocity using optical Doppler tomography,” *Opt. Lett.* **22**(14), 1119–1121 (1997).
  60. S. Chen, J. Yi, and H. F. Zhang, “Measuring oxygen saturation in retinal and choroidal circulations in rats using visible light optical coherence tomography angiography,” *Biomed. Opt. Express* **6**(8), 2840–2853 (2015).
  61. R. S. Shah, B. T. Soetikno, J. Yi, W. Liu, D. Skondra, H. F. Zhang, and A. A. Fawzi, “Visible-Light Optical Coherence Tomography Angiography for Monitoring Laser-Induced Choroidal Neovascularization in Mice,” *Invest. Ophthalmol. Vis. Sci.* **57**(9), 86–95 (2016).
  62. D. C. Lozano and M. D. Twa, “Quantitative Evaluation of Factors Influencing the Repeatability of SD-OCT Thickness Measurements in the RatSD-OCT Repeatability in the Rat,” *Invest. Ophthalmol. Vis. Sci.* **53**(13), 8378–8385 (2012).

## 1. Introduction

Optical coherence tomography (OCT) is an imaging technique based on low-coherence interferometry that provides 3-dimensional (3D) anatomic visualization of biological tissues [1, 2], with high utility in the field of ophthalmology [3, 4]. It enables a high sensitivity, high speed and non-invasive way to acquire the cross-sectional reflectivity profile of a sample [5, 6]. Besides information on the layer structure, optical coherence tomography angiography (OCTA) algorithms [7, 8] allow depth-resolved visualization of the retinal and choroidal blood circulation [9–11] and identification of abnormal vascular and blood flow changes [12] in ocular diseases such as glaucoma [13–15], age-related macular degeneration [16, 17], and diabetic retinopathy [18, 19]. Additionally, OCT has become a powerful research tool for 3D imaging of complex myocardial activities in early-stage embryonic hearts with high spatial and temporal resolution. The ability to measure blood flow velocity and myocardial wall thickness to derive wall strain in embryonic hearts is very important for fully understanding the mechanisms of cardiac development [20].

Among the various characteristics of an OCT system, good axial resolution is a fundamental concern since it determines the accuracy of image analysis in the direction of light propagation. Higher axial resolution images contain more information about the tissue under interrogation and allow better visualization of interfaces, potentially improving the accuracy and repeatability of layer boundary detection and thickness quantification in clinical applications. In the early time-domain OCT systems, the interference of the light back-scattered from the sample with the light back-reflected from a variable-length reference arm would be collected by a photodetector. Although light incoming from scatterers located at all depths in the tissue would be received, the coherence length would determine the axial resolution of the instrument. Under this OCT configuration, different positions of the reference mirror provided the information at different depths in the sample. Typically, time-domain OCT systems could provide axial resolutions of about 10-15  $\mu\text{m}$  [21, 22].

With the advent of faster Fourier-Domain OCT technology, acquisition of A-lines could be performed instantaneously with a stationary reference arm. These systems rely on either broadband detection by a spectrometer using a line-scan camera or emission by a high-speed swept-source. Owing to the availability of high-quality light sources within the water absorption window developed originally for the telecom industry, OCT systems have widely used infrared light, which is convenient in ophthalmic imaging since the patient can't see the scanning beam. Currently, the axial resolutions achievable by commercial FD-OCT systems range about 5-10  $\mu\text{m}$ : 5  $\mu\text{m}$  (Avanti RTVue-XR, Optovue), 5  $\mu\text{m}$  (Angioplex, ZEISS), 6  $\mu\text{m}$  (Maestro, Topcon) and 7  $\mu\text{m}$  (Spectralis, Heidelberg) [23–26]. Typically, higher axial resolutions have been achieved in prototypes by increasing the spectral bandwidth of the source. Resolutions of approximately 2  $\mu\text{m}$  have been obtained by broadening the light emitted by a femtosecond laser [27], since larger bandwidths allow better axial resolution (Eq. (1)). However, this is an expensive solution to achieve spectral broadening. Developments in photonic crystal fiber technology have allowed significant spectral broadenings by pumping with modest peak power laser sources, boosting the commercialization of supercontinuum sources able to provide bandwidths greater than an optical octave as well as their use as OCT sources [28]. Since ultra-broad spectra make dispersion matching between the interfering beams more challenging, moving the central wavelength to the visible spectrum is another alternative to improve axial resolution.

$$\Delta z = \frac{2 \ln 2}{\pi} \frac{\lambda^2}{\Delta \lambda} \quad (1)$$

Recently, visible light OCT (vis-OCT) has gained notoriety owing to its applicability in the field of retinal oximetry, where it takes advantage of the high hemoglobin absorption in the visible range [29–31]. Although visible light introduces discomfort in ocular imaging and is limited by a lower permissible exposure, it has been demonstrated by a Monte Carlo



simulation that oxygen saturation ( $sO_2$ ) quantification using infrared sources suffers from high inaccuracies [32]. A comparison between visible light and infrared OCT systems was performed previously [33], however the advantage of operating in the visible spectrum on axial resolution has not been exploited. As Eq. (1) shows, since the center wavelength is smaller in the visible light range, the achievable axial resolution is much higher for the same spectrum bandwidth [34] compared to OCT systems operating at 850 nm and 1310 nm. Moreover, interaction of light and biological tissue enables a stronger reflectance signal from retinal layers, at the expense of lower penetration [35].

In this work, a fiber-based OCT system that uses the visible spectrum of a commercial supercontinuum laser was built and demonstrated *in vivo* on the rodent retina and chicken embryo. High axial resolution ( $\sim 1.2 \mu\text{m}$ ) together with a motion correction algorithm allowed accurate segmentation of retinal layers, quantification of layer thicknesses in structural images, and identification of three distinct vascular plexuses within the inner retina and choriocapillaris in angiographic images. In the chicken embryo, the high axial resolution of both structural and angiographic images allowed us to quantify the thickness of large vessel walls.

## 2. Methods

### 2.1 System configuration

A supercontinuum white light laser (Super-K EXTREME, NKT Photonics) delivered ultra-broad and steady illumination over a range of 1200 nm. The light was first filtered by a short-pass and a long-pass edge filter pair (BrightLine, Semrock) with cutoffs at 496 nm and 630 nm, and coupled into a wideband 10:90 fiber optic coupler (TW560R2F2, Thorlabs) centered at 560 nm. The 10% of the power travelled to the sample arm and the other 90% travelled to the reference arm [36]. Sample arm power was set to 0.8 mW. An achromatic protected silver reflective collimator (RC08FC-P01, Thorlabs) coupled the light into free space at each arm of the interferometer. Although ideally it is the central wavelength and bandwidth of the light source that determines the axial resolution of images, in reality chromatic dispersion mismatch between the reference and sample signals deteriorates the axial point spread function [37]. In order to physically compensate most of the dispersion mismatch with the sample arm, a pair of triangular glass blocks (BK7) was placed in the reference arm and the thickness of the glass was adjustable to adapt dispersion to different samples. The reference power was further attenuated by a variable neutral density filter (NDC-100C-4M, Thorlabs) to prevent saturation of the CMOS sensor. A protected silver mirror (PF-10-03-P01, Thorlabs) was used to reflect the light back into the coupler. In the sample arm, a 2-D galvo mirror (GVS002, Thorlabs) steered the light over a squared region on the sample. A telescope formed by an objective lens ( $f = 75 \text{ mm}$ ) and ocular lens ( $f = 15 \text{ mm}$ ) was used to direct the beam to the sample. Rat retinal imaging was performed without physical contact with the cornea [38] or use of contact lenses [39]. To image the chicken embryo, a scan lens (LSM03-VIS, Thorlabs) was used to focus the scanning beam on the sample. The light collected from the sample and reference arms was spatially dispersed by an 1800 lines/mm transmission grating (Wasatch Photonics) and captured by a line scan camera (spl2048-140km, Basler) connected to a frame grabber (PCIe-1433, National Instruments). Hardware synchronization and data acquisition was controlled by custom software written in C language through a multifunction data acquisition card (USB-6353, National Instruments). The system configuration is illustrated in Fig. 1(A).

To precisely determine the working wavelengths, the spectrum was calibrated with a Neon calibration light source (NE-1, Ocean Optics) by identifying the emission lines. The spectrum centers at around 560 nm and has a full width at half maximum (FWHM) bandwidth of 90 nm (Fig. 1(B)). The theoretical axial resolution calculated from Eq. (1) is  $1.53 \mu\text{m}$ , which is 2.3 and 5.5 times better than a system operating at 850 nm and 1310 nm

with same bandwidth. The axial resolution measured experimentally as the FWHM of peaks on Fig. 1(C) was  $1.7\ \mu\text{m}$  in air, equivalent to  $1.2\ \mu\text{m}$  in tissue.

Depth range of  $1.8\ \text{mm}$  was measured by counting the pixels between the interfaces of a microscope glass slide of thickness  $200\ \mu\text{m}$  placed in the reference arm. To assess system sensitivity, a protected silver mirror was placed at different depths in the sample arm. After acquisition, one thousand A-lines were averaged at each depth (Fig. 1(C)). Considering that light passes the neutral density (ND) filter (Thorlabs, OD = 3.0) twice, the maximum sensitivity found was 89 dB, comparable to the sensitivity of systems built in free-space [33, 40]. The 6 dB roll-off depth is  $1.1\ \text{mm}$ , which is enough to cover the whole retina. Beyond this point, the sensitivity drops at a rate of  $15\ \text{dB}/\text{mm}$ .

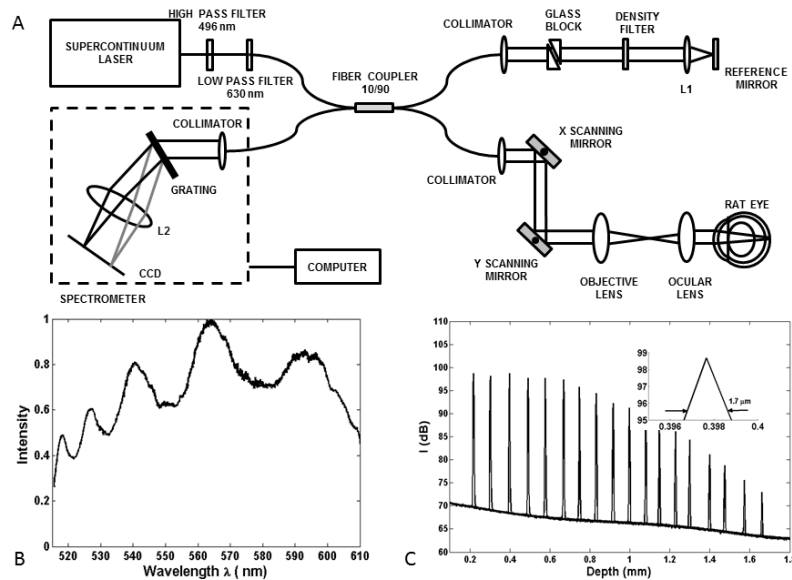


Fig. 1. (A) Schematic of the visible light optical coherence tomography (vis-OCT) system for rat retina imaging. L1, L2: Lens. (B) Calibrated spectrum in spectrometer using a Neon calibration light source. The center wavelength is  $560\ \text{nm}$  and full maximum at half width (FWHM) bandwidth is  $90\ \text{nm}$ . (C) Maximum sensitivity was 89 dB considering the light passes a neutral density (ND) filter (OD = 3.0) twice. Inset shows the measured axial resolution  $1.7\ \mu\text{m}$  in air, which is equivalent to  $1.2\ \mu\text{m}$  in tissue.

## 2.2 Animal preparation

Brown Norway rats were anesthetized using a Ketamine/Xylazine cocktail solution (25 mg/ml Ketamine, 5 mg/ml Xylazine and 1 mg/ml acepromazine). The solution was administrated via intraperitoneal injection (IP) at a dosage of  $1.5\ \text{ml}$  per kilogram of body weight. A supplementary dose (40% of the original volume) was administrated 40 minutes after the initial injection to maintain deep anesthesia. Before imaging, we dilated the pupil with a 0.5% tropicamide ophthalmic solution. The animal was immobilized on a custom-made imaging stage adjustable over five degrees of freedom. The animal's body temperature was kept warm using an electronic heating pad. The eye was frequently moisturized by a sterile irrigating salt solution (Alcon Laboratories Inc.) to prevent corneal dehydration.

For chicken embryo imaging, fertilized chicken eggs were incubated in a digital hatcher incubator at a temperature of  $37.5\ ^\circ\text{C}$  and humidity around 50%. The incubator automatically rotated the eggs every two hours to warm them homogeneously. The onset of blood circulation began on the third day and the vascular network bestrewed on the surface of the yolk sac gradually. On the 11th day, a successfully grown embryo model was picked up for experiment after examination under a flashlight. To expose the blood vessels, the eggshell was stripped with tweezers on the opposite side of the heart and the shell membrane was

peeled off to enable a direct view of the region of interest. After that, the embryo was transported to the sample stage.

All the experimental procedures were approved by the Institutional Review Board/Ethics Committee and the Institutional Animal Care and Use Committee (IACUC) of Oregon Health & Science University (OHSU).

### 2.3 Image acquisition and processing

For imaging the rat retina, an A-line rate of 50 kHz was used and  $512 \times 3 \times 512$  A-lines were scanned to form a volumetric data set. For a total of 50 fly-back points per B-frame, the time between adjacent B-scans was 11 ms and the whole volume acquisition took approximately 17 seconds to complete. For chicken embryo imaging, an area of  $1.5 \times 1.5 \text{ mm}^2$  was scanned at an A-line rate of 25 kHz and 256 A-lines were acquired in the fast transverse (X) direction to form a B-scan. Five consecutive B-scans were captured before moving to the next slow transverse (Y) position. A total of 256 locations in the Y direction were recorded within 13 seconds.

Proper focusing on the retinal tissue is critical for good-quality OCT imaging. For this purpose, the separation between the objective and ocular lenses was adjusted to correct for the eye refractive error. This was done by moving the ocular lens while the operator inspected the quality of nerve fiber layer (NFL) visualization on the *en face* mean reflectance image while scanning with low-density sampling. For real-time display of the *en face* reflectance during scanning, parallel computation on the GPU (GeForce, Quadro K420) using CUDA was incorporated into the control software written in C [41]. This method of real-time focusing assessment is more reliable than examining cross-sectional B-scans, and allowed us to easily bring the optic disc into the scanning window.

The OCT processing procedures were similar to those published previously [42]. In brief, we removed the DC component of the interferometric fringe, resampled it to be linear in the k-domain and digitally compensated the remaining chromatic dispersion. The  $z$  depth structural information was retrieved by fast Fourier Transform and averaged over the repeated frames. Angiographic images were generated using the Split-Spectrum Amplitude-Decorrelation Angiography (SSADA) algorithm [9]. SSADA splits the spectrum into  $S$  bands and calculates the decorrelation value of each band among consecutive B-scans at the same location. In this work, the full spectrum was split into eight bands of a FWHM approximately 21 nm. Given  $R$  repeated B-frames and  $A_{i,s}$  the A-line generated by the  $s^{\text{th}}$  split spectrum corresponding to the  $i^{\text{th}}$  B-scan at the same position, the final angiography  $D$  was obtained by:

$$D = 1 - \frac{1}{S(R-1)} \sum_{i=1}^{R-1} \sum_{s=1}^S \frac{2A_{i,s}A_{i+1,s}}{A_{i,s}^2 + A_{i+1,s}^2} \quad (2)$$

A directional graph search technique was employed to determine retinal layer boundaries [42]. This method takes advantage of two features of tissue layers: (1) they are primarily horizontal structures on B-scan images and (2) boundaries propagate assuming an anisotropic probability for neighboring voxels. The boundaries are further enhanced by calculating the intensity gradient in depth along the A-line. When searching for the optimal connection of a boundary, the segmentation algorithm considers 5 directional neighbors and minimizes the overall cost function.

## 3. Rat retina imaging

### 3.1 Motion correction

Even under deep anesthesia, eye bulk motion due to breathing and the cardiac cycle can be significant, given the high axial resolution of the system. Motion distorts the retinal layer boundaries when averaging the B-scans acquired at each position, and increases the

background noise on the angiographic data which overwhelms blood vessel signals and show line artifacts on *en face* images [43, 44].

We implemented a motion correction algorithm (Fig. 2(A)) to enhance the quality of both structural and flow images. First, for the B-scans at a  $y$  location, the center of mass ( $z_c, x_c$ ) was obtained. Then, the B-scans depths were cropped to form a  $200 \times 512$  pixels image around the center of mass that contains only the tissue region in order to decrease confounding effects from noise and reduce the computation time. After that, a 2 dimensional cross-correlation was calculated between the 1st and  $i^{\text{th}}$  cropped B-scans, and the misalignment was determined by the location of the maximum value in the cross-correlation matrix. Lastly, the B-scans were co-registered by shifting back the  $i^{\text{th}}$  B-scan along  $z$  and  $x$  directions.

A remarkable qualitative improvement was achieved for the averaged B-scans at the same  $y$ -location after the bulk motion correction. Retinal layers were more distinct than without motion correction (Fig. 2(B1)), especially the external limiting membrane (ELM) and the Bruch's membrane (BM) (Fig. 2(B2)). The distinct boundaries of each layer better illustrate the structure of the retina and makes segmentation easier. Compared to imaging by systems operating at longer wavelengths [39, 45], retinal imaging exhibited some unique features in vis-OCT. Increased layer contrast was obtained owing to the stronger interaction between light and tissue, caused by the relative high scattering coefficient of tissue in the visible range. In OCTA processing, the correction obtained from full-spectrum OCT was applied on the split-spectrum OCT before the decorrelation was computed. Bulk motion artifacts were also largely suppressed with motion correction algorithm (Fig. 2(C1)-2(C2)).

It was also observed that shadows cast by large vessels in B-scans were darker in vis-OCT than in systems that operate with infrared illumination [46, 47]. The intensity of an A-line crossing a large blood vessel attenuates quickly and no angiography data are extracted underneath. This also prevents visualization of projection artifacts of superficial flow in deeper vascular plexuses (Fig. 2(C1)-2(C2)).

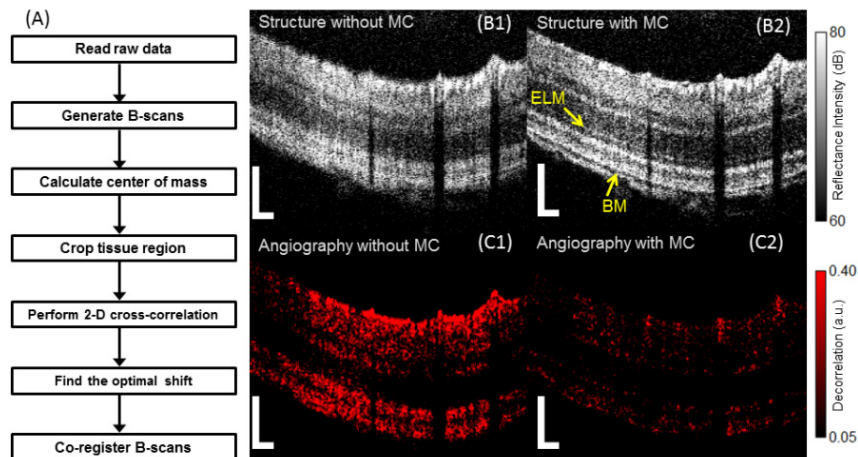


Fig. 2. (A) Motion correction algorithm based on cross correlation of cropped B-scans. (B1) A B-scan without motion correction. The tissue appeared blurred and the boundaries were unclear. (B2) The structural B-scan with motion correction. The visualization of layers is enhanced, especially for the external limiting membrane (ELM) and Bruch's membrane (BM). (C1) The corresponding angiography B-scan for structure B-scan in B1. The noise level is high since bulk motion exists between the B-scans. (C2) Angiography B-scan after motion correction. Observe that noise in avascular tissue is largely suppressed. Scale bar = 100  $\mu\text{m}$ .



### 3.2 Retinal layer thickness assessment

Accurate detection of retinal layer boundaries and quantification of their thicknesses, particularly the nerve fiber layer (NFL), are of great significance and may help the early diagnosis and progression assessment of diseases such as glaucoma, Alzheimer and Parkinson disease [48–50]. Automated segmentation of structural B-scans was applied successfully and the boundaries of seven retinal layers were identified (Fig. 3(A)); namely, the NFL, inner plexiform layer (IPL), inner nuclear layer (INL), outer plexiform layer (OPL), outer nuclear layer (ONL), inner and outer photoreceptor segment (IS/OS) and retinal pigment epithelium (RPE). The structural and angiographic images were flattened according to the IS/OS boundary (Fig. 3(B)) and averaged depth profiles were obtained (Fig. 3(C)). Inspection of the angiographic z-profile showed three distinct retinal plexuses: superficial vascular plexus (SVP), intermediate capillary plexus (ICP) and deep capillary plexus (DCP), resembling the axial vascular distribution of the human retina [51–53] and mouse retina [54]. Below Bruch's membrane, the flow signal from the choriocapillaris was detected.

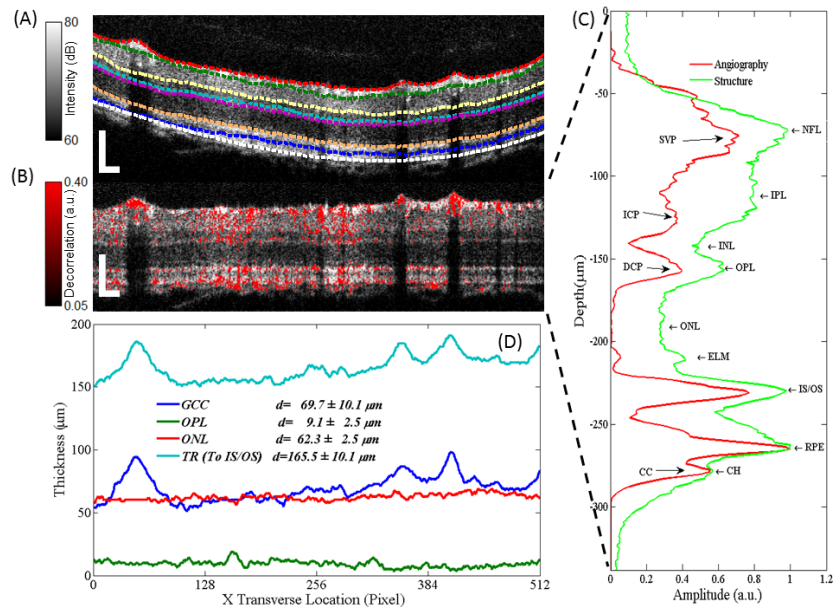


Fig. 3. (A) B-scan cross section of rat retina with layer boundaries segmented. (B) Flattened structural B-Scan overlapped with angiography. (C) Averaged structure and angiography z-profiles. The structural z-profile (green curve) displayed the reflectance variation of layers, where the NFL, IS/OS and RPE appeared as the brightest layers in the retina and the ONL was the darkest. The angiography z-profile (red curve) showed peaks at three distinct inner retinal plexuses and choriocapillaris. NFL: nerve fiber layer, IPL: inner plexiform layer, INL: inner nuclear layer, OPL: outer plexiform layer, ONL: outer nuclear layer, ELM: external limiting membrane, IS/OS: inner and outer photoreceptor segment, RPE: retinal pigment epithelium, CC: choriocapillaris. SVP: superficial vascular plexus, ICP: intermediate capillary plexus and DCP: deep capillary plexus. (D) The thicknesses of GCC, OPL, ONL and total retina calculated from the segmentation results. ELM thickness could not be measured with this method. GCC: ganglion cell complex, TR: total retina. Scale bar = 100  $\mu\text{m}$ .

We further assessed the thicknesses of the ganglion cell complex (GCC, i.e. NFL + GCL + IPL), OPL, ONL and total retina layers based on the segmented boundaries. The thickness of the OPL and ONL was uniform along the X transverse locations (Fig. 3(D)). Conversely, the thickness of GCC and total retina varied along X transverse locations due to large superficial vessels. The averaged thicknesses, as well as the standard deviations (SD) for GCC, OPL, ONL and total retina were  $69.7 \pm 10.1 \mu\text{m}$ ,  $9.1 \pm 2.5 \mu\text{m}$ ,  $62.3 \pm 2.5 \mu\text{m}$  and  $165.5 \pm 10.1 \mu\text{m}$ , showing consistency with measurements made using other systems [39].

To investigate the NFL thickness characteristics, two repeated volumetric scans were taken on four rats. NFL and OPL thickness maps were generated for each scan, registered and averaged (Fig. 4). After masking large blood vessels, the NFL thickness appeared larger at positions closer to the optic disc in all four rats. In contrast, the OPL thickness was uniform in the whole image. Moreover, unlike in the human retina, the NFL distribution pattern in the rat displayed a ‘crescent’ pattern, in which the NFL was thicker in one side of optic disc than the other side even at the same distance. However, the rat retina does not have a macula and the disc vascular network is different with human retina. Although it is recognized that retinal artery and vein enter the rat eye lying inferior to the optic nerve head [55], it is not possible to actually visualize the nerve head itself. Therefore, we couldn’t draw a solid conclusion about the exact location of the thicker part.

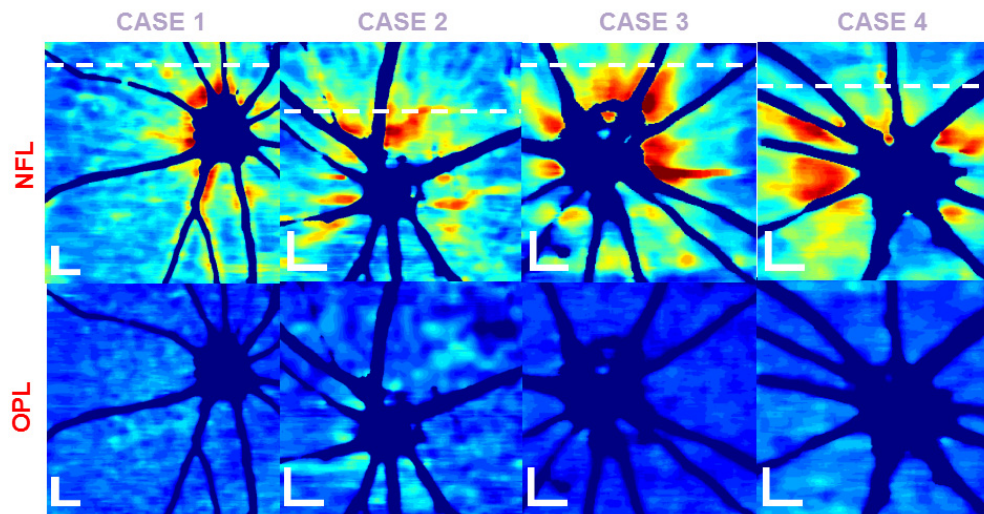


Fig. 4. NFL and OPL thickness maps for four different rats. The NFL thickness was larger near the disc and showed a ‘crescent’ distribution pattern. In contrast, the OPL thickness appeared uniform. Dashed white line represents B-scans at the same distance from the optic disc. Scale bar = 300  $\mu\text{m}$ . color map: [5  $\mu\text{m}$ , 45  $\mu\text{m}$ ].

Table 1. NFL and GCC thickness measurement

Case	NFL ( $\mu\text{m}$ )			GCC ( $\mu\text{m}$ )		
	A	B	MEAN $\pm$ SD	A	B	MEAN $\pm$ SD
1	24.2	23.3	23.75 $\pm$ 0.64	76.5	75.9	76.20 $\pm$ 0.42
2	27.0	26.8	26.90 $\pm$ 0.14	75.3	77.0	76.15 $\pm$ 1.20
3	39.3	40.1	39.70 $\pm$ 0.57	84.0	82.8	83.40 $\pm$ 0.85
4	29.6	29.9	29.75 $\pm$ 0.21	88.5	88.7	88.60 $\pm$ 0.14

SD: standard deviation

In order to validate the repeatability of thickness measurements, a B-scan at the same distance from the optic disc was chosen from each scan (Fig. 4). From Table 1, the inter-scan repeatability (pooled standard deviation) of the NFL and GCC thickness measurements were 0.45  $\mu\text{m}$  and 0.77  $\mu\text{m}$ , respectively. The population variations (coefficient of variation) of these two measurements were 23.0% and 7.5%, respectively. These large variations between animals suggest that, although the selected B-scans were at the same distance to the optic disc, they were located at different positions in relation to the crescent pattern, thus exhibiting different NFL thickness variability. This proves that the NFL thickness does not equally decrease radially in all directions and is evidence to the ‘crescent’ distribution pattern in the rat retina.

### 3.3 Vis-OCT angiography

As mentioned previously, the inner retina could be divided into three vascular/capillary plexuses: SVP, ICP and DCP (Fig. 5). The SVP was located in the layers of NFL, GCL and inner section of the IPL; the ICP was between the outer IPL and inner INL, and the DCP was found between the outer INL and OPL (Fig. 3(C)). The angiograms were displayed by maximum projection of the volumetric flow data into an *en face* image. The large blood vessels noticeable in the SVP were distributed radially from the optic disc. Capillaries down to the fifth branch level could be visualized. The microvascular networks in the ICP and DCP reveal different vascular patterns, corresponding to the histological findings [56] (Fig. 5(E)). It should be noted that the choriocapillaris could be observed and projection artifacts imposed on the DCP, ICP and choriocapillaris caused by flow in the SVP were very minimal.

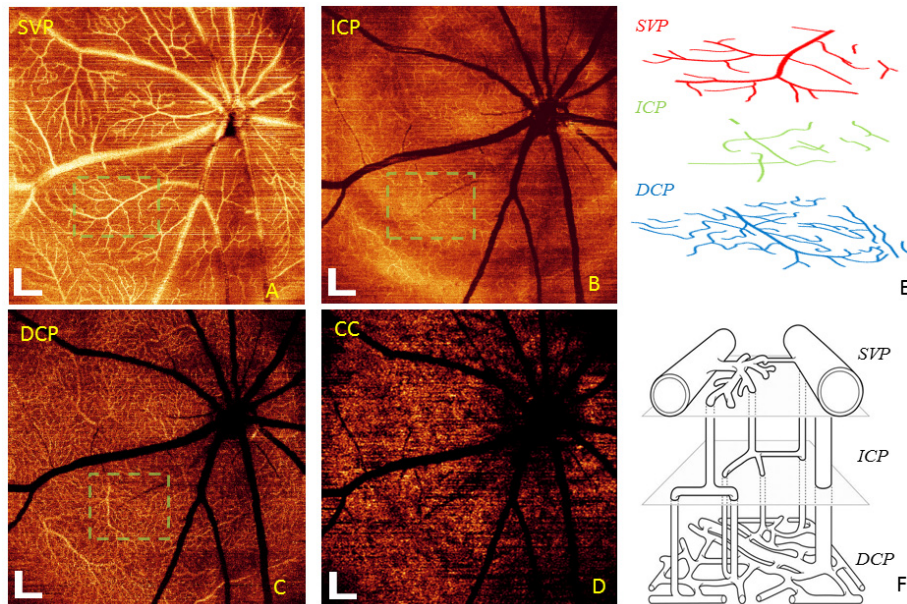


Fig. 5. 3.2mm  $\times$  3.2mm *en face* angiograms generated by the maximum projection of the flow data contained in the SVP (A), ICP (B) and DCP (C) vascular plexuses of the inner retina and choriocapillaris (D). Enlarged vascular networks (E) in SVP, ICP and DCP from the green dashed boxes in A, B and C correspond to the histology of micro vessels in the inner retina (F, Reprinted with permission from Paques [56].) Scale bar = 200  $\mu$ m.

### 4. Chicken embryo imaging

Study of chicken embryo models provide easily accessible *in vivo* blood flow while sharing great similarities with mammalian embryology [57]. Before imaging, the egg was carefully tilted to avoid specular reflection from the egg white and vitelline membrane (Fig. 6(A)). Surrounded by various high reflective matters within the *yolk*, the microvascular network looks dim in the structural *en face* mean projection (Fig. 6(B1)), exhibiting a very low contrast with surrounding tissue. In *en face* maximum projection of angiographic image (Fig. 6(B2)), distinct microvasculatures were visualized.



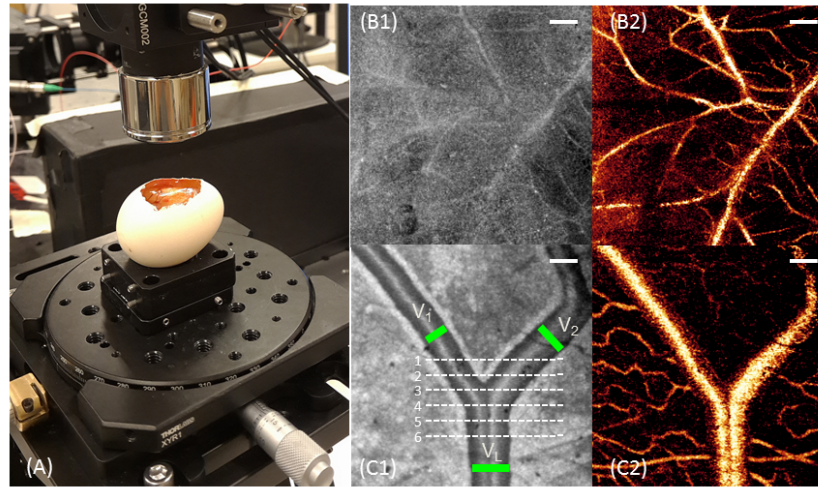


Fig. 6. In vivo chicken embryo imaging with vis-OCT. (A) Photograph of the sample arm. The fertilized egg was placed in a vertical stage with blood vessels exposed for imaging. (B1) *En face* mean structural projection of microvascular network. (B2) *En face* maximum angiographic projection of microvascular network. (C1) *En face* mean structural projection of a venous bifurcation. White dashed lines indicate the B-scan positions in Fig. 7 and green lines indicate the diameters of three branches of bifurcation. (C2) *En face* maximum angiographic projection of a venous bifurcation. Scale bar = 200  $\mu\text{m}$ .

In this sample we examined a venous bifurcation. The bifurcation is highly remarkable in both reflectance (Fig. 6(C1)) and angiography (Fig. 6(C2)) *en face* visualization. However, angiography reveals the deep capillaries concealed behind avascular tissue in the structural image. The outer diameters of parent ( $V_L$ ) and daughter branches ( $V_1$  and  $V_2$ ) were measured in the structural *en face* images at five positions in the vicinity of the green bars represented in Fig. 6(C1). Results (Table 2) are in agreement with Murray's law [58], which states that there is a cubic relationship between diameters of daughter branches and parent branch.

**Table 2. Diameters and wall thickness of the parent and daughter branches of a venous bifurcation in chicken embryo.**

Measurement	$V_1$	$V_2$	$V_L$
Outer Diameter ( $\mu\text{m}$ )	$170.1 \pm 5.3$	$208.9 \pm 7.1$	$243.1 \pm 3.5$
Wall thickness ( $\mu\text{m}$ )	$12.6 \pm 0.9$	$11.0 \pm 1.6$	$19.1 \pm 1.1$

It is also noted from the *en face* image that the flow in branch  $V_L$  exhibits a spindle shape at the beginning of the merging and the flow follows the daughter branches for some distance before merging together (Fig. 6(C2)). This laminar behavior is unique in vein bifurcations and can be explained by hemodynamics analysis. Six B-scans near the bifurcation were selected to demonstrate this phenomenon cross-sectionally (Fig. 7). In B-scans #3, #4 and #5, it is clear that the spindle shape observed *en face* resulted from the laminar flow rather than a vessel wall.

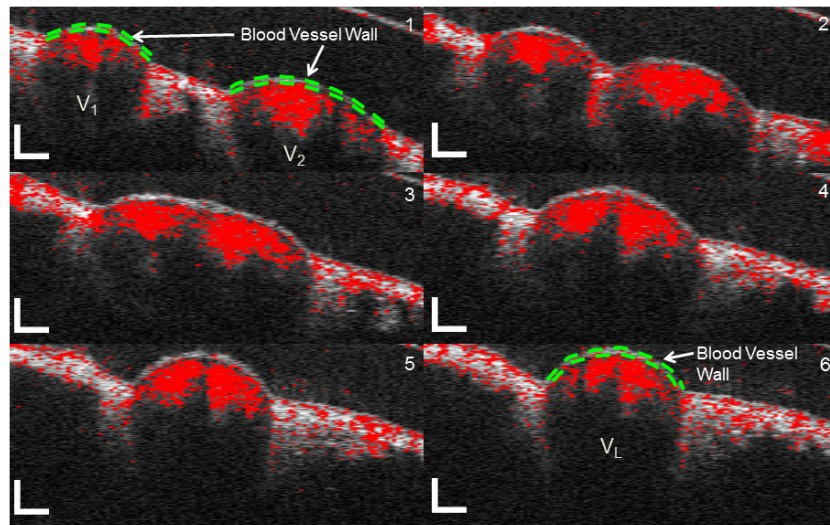


Fig. 7. B-scans around the bifurcation illustrate the situation of two daughter veins merging into a larger vein in chicken embryo. A laminar behavior is observed. With angiography overlapped in the reflectance image, the blood vessel wall is clearly identified and the thicknesses could be calculated by segmenting the inner boundary and outer boundary of the blood vessel. Scale bar = 100  $\mu\text{m}$ .

Blood vessels walls could be clearly distinguished on structural B-scans overlapped with angiography (Fig. 7), similar to the findings in Ref [59]. Here, owing to the high axial resolution of vis-OCT, the inner boundary and outer boundary of large vessel walls could be segmented, as indicated by the green dashed lines in B-scans #1 and #6. The wall thicknesses of  $V_1$ ,  $V_2$  and  $V_L$  were measured between the inner and outer boundaries at five separate B-scans located in the vicinity of positions #1 and #6 respectively.

## 5. Discussion and conclusion

A fiber-based vis-OCT was designed to achieve angiographic and structural imaging in biological tissue at high axial resolution. When imaging the rat retina, layer boundaries were accurately segmented and the NFL thickness could be measured with good repeatability. In the averaged angiographic z-profile, three retinal vascular plexuses and choriocapillaris were observed, their positions had good correspondence with the plexuses found in human retina and their vascular networks were distinct. Although vis-OCT penetration is less than conventional OCT in the near infrared band, the choriocapillaris could still be detected. The field of view of angiography images was larger than previous reports of visible-light OCTA [30, 60, 61]. When imaging chicken embryo, the microvascular and a venous bifurcation were investigated and a laminar behavior was observed near a venous bifurcation. By overlapping the structure and angiography B-scans, blood vessels wall thickness could be easily appreciated and computed.

Here, volumetric structural OCT analysis of the NFL thickness was completed and a detailed distribution pattern was demonstrated for the first time in rodents, to the best of our knowledge. Previously, Ref [62], measured the NFL thickness at 16 discrete B-scan distances from the optic disc and found that it varied from 19  $\mu\text{m}$  to 29  $\mu\text{m}$ . Later, the NFL thickness map at the temporal region of rat retina was achieved [39] showing a radially distributed thickness but failing to reveal the ‘crescent’ distribution pattern around the whole disc. In this work, the axial resolution provided by vis-OCT and masking of the large vessels allowed us to observe this feature in better detail.

From their inception, OCTA algorithms have been applied on systems operating with infrared light and researchers have struggled to remove the projection artifacts observed in the



intermediate and deep capillary plexuses, caused by the fluctuating shadows cast by blood cells moving in the more superficial vessels. Although four retinal capillary plexuses in human retina have been reported [52], a projection-resolved algorithm [51, 53] has to be applied. By using vis-OCT, projection artifacts of superficial capillary flow were not discerned in the deeper plexuses, presumably because of the combination of stronger reflectance in capillaries located at deeper layers and larger attenuation of the projected superficial flow at visible light wavelengths. Compared to OCTA using infrared light sources, visible light OCTA is more resistant to projection artifacts. However, the stronger absorption of light by large superficial vessels causes darker shadow artifacts than those observed with infrared illumination, which hinders retrieving the angiographic signal when the reflectance amplitude is at the level of the background signal.

Visible light OCT appears to enable “true” depth-resolved OCTA, but suffers motion artifacts as well as current OCT systems. In this study, the motion correction algorithm based on the cross correlation of two cropped B-scans effectively reduced the prevalence of eye motion, predominately caused by cardiac pulses and respiration. However, this algorithm would not be able to fix events of micro-saccadic motion.

In summary, the high-axial resolution of vis-OCT can help quantify more accurately layer thickness, useful in the assessment of glaucoma, Alzheimer’s and Parkinson’s disease. It also helps reduce the effect of projection artifact, allowing visualization of the different plexuses in depth-resolved angiography with resolution similar to the capillary diameter, as well as visualization of the choriocapillaris. Given that most of the investigations using vis-OCT are still performed in rodents, the similarity of the axial distribution of their retinal flow to humans revealed here confirms the benefits of rodent models in clinical research. The ability to calculate vessel diameter and wall thickness suggests vis-OCT can also assist the investigation of biomechanics’ role on embryonic cardiac development better than systems operating with infrared illumination.

### Funding

This work was supported by grant R01 EY027833, DP3 DK104397, R01 EY024544, R01 EY023285, R01 EY010145, P30 EY010572 from the National Institutes of Health (Bethesda, MD), and an unrestricted departmental funding grant and William & Mary Greve Special Scholar Award from Research to Prevent Blindness (New York, NY).

### Disclosures

David Huang: Optovue Inc (F, I, P, R, S). Yali Jia: Optovue Inc (P). Miao Zhang: Optovue Inc (E). These potential conflicts of interest have been reviewed and managed by OHSU. Other authors declare that there are no conflicts of interest related to this article.